A Machine Learning Approach to Detection of Geomagnetically Induced Currents in Power Grids

Shiyuan Wang ⓘ , *Student Member, IEEE*, Payman Dehghanian ⓘ , *Member, IEEE*, Li Li ⓘ , *Student Member, IEEE*, and Bo Wang ⓘ , *Student Member, IEEE*

Abstract—**Geomagnetically induced currents (GICs) in power grids are mainly caused by geomagnetic disturbances especially during solar storms. Such currents can potentially cause negative impacts on power grid equipment and even damage the power transformers resulting in a significant risk of blackouts. Therefore, monitoring GICs in power systems and developing solutions to mitigate their impacts before rising to a certain threatening level is urgently in need. Monitoring GICs is, however, quite a challenge and costly, as they usually appear in forms of dc components in the high voltage transmission lines, which are barely accessible through transformers. By examining the measured currents from the current transformers, this article proposes a framework to detect GICs in power transmission systems through a hybrid time-frequency analysis combined with machine learning technology. Simulated results verify that the proposed approach can promisingly estimate GICs in power systems during a variety of grid operating conditions.**

Index Terms—**Convolutional neural network (CNN), feature extraction, geomagnetic disturbance (GMD), geomagnetically induced current (GIC), harmonics, wavelet transform (WT).**

I. INTRODUCTION

GEOMAGNETIC disturbances (GMDs) are mainly caused by solar storms, during which charged particles erupt from solar flares resulting in coronal mass ejections into space during the intensity peak of the sun's cycle. Consequently, geomagnetically induced currents (GICs) will appear in the conductor surface of the Earth. The flow of these currents into power transmission lines can potentially cause "half-cycle saturation" of high-voltage bulk power transformers. This phenomenon can lead to relay missoperations, voltage dips, elevated reactive power demand, transformer overheating, disruptive harmonics, aging or malfunction of the electric power devices, and even a total collapse of the grid in the worst scenarios [1]–[5].

Northern North America is particularly susceptible to problems resulting from GICs. On March 13, 1989, an exceptionally

strong GMD caused major damages to electrical power equipment in Canada, Scandinavia, and the United States. Hydro-Quebec extra high voltage (EHV) transmission system experienced instability and tripping of lines carrying power to Montreal resulting in the total blackout of the Hydro-Quebec system [6], [7]. In the United States, a voltage fluctuation of up to 4% was recorded on the EHV systems in Pennsylvania, New Jersey, and Maryland. On September 19, 1989, a second solar storm damaged the step-up transformers at the Salem Unit 2 nuclear power plant [8].

Limiting the potential GICs-caused damages in power grids calls for developing advanced tools and mechanisms to monitor and detect GICs as they unfold and also solutions to mitigate the impacts before they rise to a certain threatening level. On one hand, the GMD phenomena may not always result in GICs in power systems. On the other hand, directly accessing GICs—which represents itself as a dc component in high voltage transmission lines—is costly and a challenge. Conventional techniques to monitoring high voltage transmission lines rely solely on the ac measurements through voltage transformers (VTs) and current transformers (CTs), simply neglecting the dc components flowing on transmission lines. Additionally, there are other sources of harmonics in power grids, generated by nonlinear loads or overloading transformers, that may flow in the grid [9] and can interfere with those harmonics generated by GICs, particularly when GMD level is low. Such interference will make the GICs detection a challenge, as the measured waveforms from CTs or VTs capture all harmonic signals together with the fundamental component—50 or 60 Hz.

Several studies have focused on modeling harmonic-embedded power flows and mitigation solutions when facing GICs in power systems [2], [10]–[12]. Different mitigation strategies should be taken depending on the severity of GICs impacts on the grid. However, research and development efforts on GICs impact detection mechanisms are found scarce. The proposed techniques in [13] and [14] are centered on monitoring GICs mainly based on analyzing the distorted waveforms; however, none has considered the appearance of other grid harmonics and the conflicting interactions with those of GICs. Furthermore, thermal noise would be higher in the transformer secondary winding due to the accumulated heat during transformer saturation, which adds another layer of interference, making GICs detection harder than usual. Additionally, studies in [3] demonstrated that the excited harmonic current magnitudes of different orders vary when GICs intensity increases.

The harmonic components generated by GICs behave in different ways and the existing detection mechanisms do not consider such complex interference.

Studies in [9] show the promising performance of transformer overloading detection by applying wavelet transforms (WT). Machine learning mechanisms have been widely utilized in solving electric power system problems [15]–[18] and are being frequently approached to revolutionize the solution techniques and emerging technologies in power grids. Inspired by the principle concepts of feature extraction and event detection based on waveform analysis, this article proposes a GIC detection solution in high voltage transmission systems. Two major time-frequency analysis techniques, namely the WT and short-time Fourier transform (STFT), are applied and their performance are evaluated. We further propose a GIC detection algorithm centered on a hybrid WT and STFT combined with a machine learning approach, convolutional neural networks (CNN). We demonstrate the promising performance of the suggested analytics in detecting the GIC impacts in power grids under a variety of grid operating conditions. The proposed framework, first, is resistive to harmonic distortion and background noise, second, is capable of detecting low-intensity GICs, and third, can be algorithmically embedded within phasor measurement units (PMUs) and other intelligent electronic devices (IEDs) currently in place for online monitoring.

The rest of this article is organized as follows. Section II introduces the GICs impact modeling and the motivation to feature extraction based on STFT and continuous WT. Section III describes the proposed online GICs detection framework, consisted of feature extraction from the current signals via the pseudocontinuous wavelet transform (PCWT) and event classification via CNN. Case studies and experimental results are analyzed in Section IV to verify the performance of the proposed GICs detection mechanism. Finally, this article is concluded in Section V.

II. BACKGROUND AND MOTIVATION

A. Overview of GICs Modeling

The GMD phenomenon introduces an earth magnetic field change rate of usually below 1 Hz [2]. Typically, GICs can be determined by assessing the dc network power flow as

$$\mathbf{I} = \mathbf{G}\mathbf{V} \tag{1}$$

where $\mathbf{G}$ is the network bus admittance matrix, determined by taking into account the three-phase signals, the substation neutral buses, as well as the ground resistances. Utilizing the approach presented in [1], the GMD introduces voltages that can be approximated by

$$V = E_N L_N + E_E L_E \tag{2}$$

where E_N and E_E are the Northward and Eastward electric field (V/km), respectively, and L_N and L_E are the Northward and Eastward distance, respectively.

In transmission systems, Y–Y configuration transformers are the most vulnerable to half-cycle saturation during a GMD event. As graphically demonstrated in Fig. 1, this is because the dc
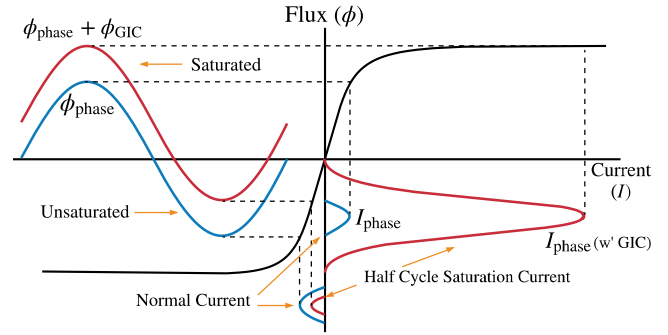

Fig. 1.   Half-cycle saturation of a single-phase transformer due to GICs.
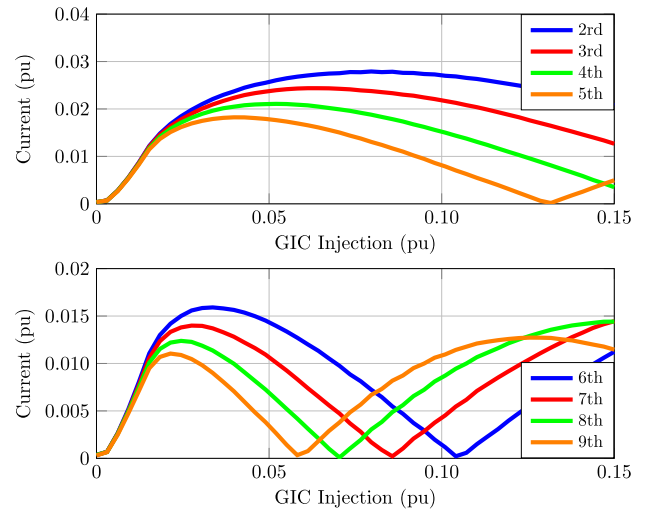

Fig. 2.   Excited harmonic current components in different levels of GICs.

flux has the lowest reluctance path in such scenarios and a semisaturation can occur [19]. However, GICs alone may not be able to cause a transformer half-cycle saturation as GICs intensity may be low and the transformer load level may be small. According to [3], when a transformer is injected with different levels of GICs, the harmonic magnitude curves (in frequency domain) will differ significantly (see Fig. 2), thus the waveforms will change dramatically too. Such behaviors in the waveforms will make the GICs detection process extremely difficult, calling for a holistic mechanism and an accurate approach.

B. Power Waveform Modeling

As the current in the secondary winding of CTs can be captured and assuming a balance three-phase system, the power waveform in each phase can be represented as follows:

$$x(t) = A \cos(\omega t + \phi) \tag{3}$$

where $x(t)$ is the measured one-dimension (1-D) waveform; A, ω, and ϕ are the instantaneous magnitude, fundamental frequency, and phase angle in each phase, respectively. Although GICs cannot be measured directly, their impacts can be assessed on the dc saturation level of transformers as GICs generates a set of harmonic components only during the transformer half-cycle
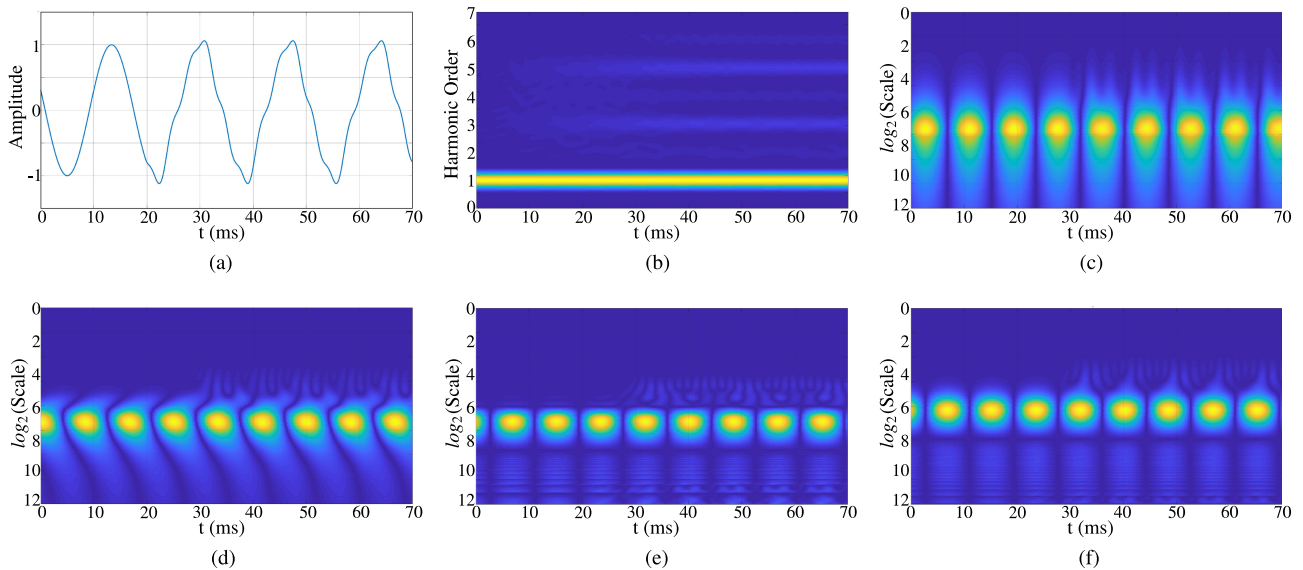
Fig. 3.   Comparison of the STFT versus WT: harmonic injection starts at $t = 20$ ms, with harmonic orders $h = 2, 3, 4, 5, 6$ and magnitude of 0.02, 0.08, 0.02, 0.08, and 0.02 p.u., respectively. (a) Waveform. (b) STFT. (c) Haar. (d) DB4. (e) Morlet. (f) Gaussian.

saturation. Thus, the waveform can be expanded by Fourier series as

$$x(t) = A_1 \cos(\omega_1 t + \phi_1) + \underbrace{\sum_{h=2}^{H} A_h \cos(\omega_h t + \phi_h)}_{\text{Harmonic Components}} \quad (4)$$

where h is the order of harmonics; and H is the maximum order of harmonic of interest. Under a particular level of GICs, different values of A_h and f_h can be detected according to [3], resulting in a unique set of patterns. A certain combination of A_h for ω_h (for $h = 2, 3, 4, ..., \text{H}$) will possibly be resulted, even if some GICs-caused harmonics are influenced by those generated from other sources. The second term in (4) will still contain valuable information on the GICs impacts and, thus, could be the main target for data fusion and pattern extraction.

For time–frequency analysis of the waveforms, STFT [20], [21] would be one promising approach facilitating the GICs impact detection. The STFT offers a high measurement accuracy at the cost of high computational complexity [22], [23]. Meanwhile, according to [24]–[29], WT has shown speed advantages over the STFT in time–frequency analysis, especially when applied for feature extractions. The performance of different time–frequency analysis techniques are demonstrated and compared in Fig. 3. It can be seen from the spectrum in Fig. 3(b) and scalograms in Fig. 3(c)–(f), that the feature extraction outcomes through WT are much more conspicuous than those of STFT, while compromising the accuracy in frequency measurements. Therefore, a joint hybrid application of WT and STFT is pursued in this article for waveform feature extraction and the corresponding analysis.

C. WT and Pseudocontinuous WT

The WT of a 1-D waveform is achieved by computing the cross correlation between the signal of interest $x(t)$ and

designated wavelets. This process is defined by the following equation:

$$X(\omega|a, b) = \frac{1}{\sqrt{a}} \int_{-\infty}^{\infty} x(t) \Psi\left(\frac{t-b}{a}\right) dt \quad (5)$$

where $\Psi(t)$ is the mother wavelet when the scaling factors $a = 1$ and the time shift $b = 0$ are set. $\Psi(\frac{t-b}{a})$ is the "daughter wavelets" of $\Psi(t)$ with different selection of a and b [25], [26]. In real applications where the discrete signal processing is applied, both the integration interval and the number of scaling factors are finite. Let the discrete scaling factors $a_k = 2^i$, where i is chosen from a set of linearly increasing real numbers instead of integers; therefore, the WT becomes *pseudocontinuous* (PCWT). Here, the PCWT is defined as follows:

$$X[\omega|a_k, b_k] = \frac{1}{\sqrt{a}} \sum_{n=0}^{W-1} x[n] \Psi\left[\frac{nT_s - b_k}{a_k}\right] \quad (6)$$

where T_s denotes the sampling interval, and W stands for the window (buffer) length. When applying PCWT, choosing a proper wavelet and tuning the parameters correctly are crucial as they will significantly affect the PCWT performance. Furthermore, a set of proper parameters would reduce the computational burden and improve the time efficiency, since the online feature extraction mandates real-time considerations when designing PCWT.

D. Convolutional Neural Networks

Once the features from the power waveforms are extracted, CNNs can be used as an event detector. CNNs are artificial neural networks that are primarily used to classify images based on their contents. The process mainly focuses on representation learning, meanwhile this process adapts the feature extractor automatically and has proven successful in a wide range of

image-related tasks [30]–[32]. In general, the implementation of the convolutional networks is achieved by calculating cross correlations as defined in the following equation:

$$s^p(m,n) = \sum_u \sum_v \sum_w I^u(m+v, n+w)K^p(v,w) \quad (7)$$

where $s^p(m,n)$ denotes the output of the convolutional layer at position (m,n) and pth channel, K^u is the uth convolutional kernel, and I^u represents the uth channel of the image/data volume. A complex convolutional layer consists of small number of basic layers [33] and can be expressed by the following functions:

$$I_l = \text{pool}\left(\sigma(s)\right) \quad (8)$$

where I_l represents the output volume of the lth layer, $\sigma(\cdot)$ denotes a nonlinearity of the neurons, and pool$(\cdot)$ is a pooling (down sampling) procedure. By stacking the convolutional layers, the abstraction level of the network generally increases [34]. The representations in the last layer in a CNN are usually expanded to vectors and fed into the general fully connected (FL) layers. Cross entropy is then used as the loss function.

III. PROPOSED FEATURE EXTRACTION AND GIC DETECTION BY CNNs

As single-phase CTs receive the current waveforms from the transmission lines, the GIC impacts can be evaluated through CTs located in different substations. In this section, the assessment focuses on one CT modeled based on the considerations presented in Figs. 1 and 2. The approach is, however, generic enough to be applied to different models and number of CTs across the system. Moreover, the CNNs are able to generalize and adaptive to different CT parameters, as long as the waveforms obtained from a specific CT are included in the training data set.

As wavelet transformations can be considered a special type of convolution, it is possible to integrate the feature extraction phase of the proposed approach into the CNNs. Some literature suggested using wavelets to replace the kernels of the first layer in CNNs [35], [36] and advocate a better performance than that resulted from the conventional CNNs [37]. However, the waveforms in power systems are 1-D and very different from the 2-D natural images which are featured by edges or spots, etc.; additionally, wavelet analysis is a mature approach that can extract informative features from the power waveforms; we, therefore, choose a two-phase scheme (wavelets + CNN) in our proposed framework.

A. PCWT-Based Feature Extraction During Transformer Half-Cycle Saturation

Based on the half-cycle saturation waveform in Fig. 1, which is a Gaussian-like curve, the Gaussian wavelet is a natural candidate for the mother wavelet. A Gaussian wavelet can be expressed as follows:

$$g_n(x) = (-1)^n \frac{d^n}{dx^n} e^{-\frac{x^2}{2}} \quad (9)$$

where n is the order of the Gaussian wavelet [38]. According to (5), the WT with Gaussian mother wavelet can be expressed as follows:

$$X_g(\omega|a,b) = \frac{1}{\sqrt{C_{g_n}}} \int_{-\infty}^{\infty} x(t) g_n\left(\frac{t-b}{a}\right) dt \quad (10)$$

and

$$C_{g_n} = 2\pi(n-1)!. \quad (11)$$

When conducting the Nth order Gaussian WT, (10) can be simplified by applying partial integration multiple times (see Appendix A for more details), and (10) changes to

$$X_g(\omega|a,b)$$
$$= \underbrace{\frac{1}{\sqrt{C_{g_N}}} \sum_{n=0}^{N-1} \left[\left(-a^n \frac{d^n}{dt^n} x(t) \frac{d^{(N-n)}}{dt^{(N-n)}} g_0\left(\frac{t-b}{a}\right)\right)\right]_{-\infty}^{+\infty}}_{\text{zero}}$$
$$+ \frac{1}{\sqrt{C_{g_N}}} \int_{-\infty}^{\infty} a^N \frac{d^N}{dt^N} x(t) g_0\left(\frac{t-b}{a}\right) dt. \quad (12)$$

As $x(t)$ consists of sinusoidal waveforms only, for a given frequency ω_h with A_h and θ_h, (12) can be rewritten as

$$X_g(\omega_h|a,b) = \frac{A_h a^N}{\sqrt{C_{g_N}}} \int_{-\infty}^{\infty} \frac{d^N}{dt^N} \cos(\omega_h t + \theta_h) \cdot e^{\frac{-(t-b)^2}{2a^2}} dt$$
$$= \frac{A_h a^N}{2\sqrt{C_{g_N}}} \int_{-\infty}^{\infty} \frac{d^N}{dt^N} \left[e^{j(\omega_h t+\theta_h)} + e^{-j(\omega_h t+\theta_h)}\right] e^{\frac{-(t-b)^2}{2a^2}} dt. \quad (13)$$

By applying the Hubbard–Stratonovich transformation [39]

$$\sqrt{2\pi\alpha} \cdot e^{-\frac{\alpha}{2}x^2} = \int_{-\infty}^{\infty} e^{-\frac{y^2}{2\alpha^2} - jxy} dy \quad (14)$$

and using the rule of sign change when swapping integration limits, (13) can be simplified by substituting $y = t - b$

$$X_g(\omega_h|a,b)$$
$$= \frac{A_h (a\omega_h)^N}{\sqrt{C_{g_N}}} \cos\left(\omega_h b + \theta_h + \frac{N\pi}{2}\right) \int_{-\infty}^{\infty} e^{-\frac{y^2}{2a^2} - j\omega_h y} dy$$
$$= \frac{A_h (a\omega_h)^N}{\sqrt{(N-1)!/a}} \cos\left(\omega_h b + \theta_h + \frac{N\pi}{2}\right) e^{-\frac{a}{2}w_h^2} \quad (15)$$

ω_h, A_h, θ_h are constants for one harmonic component, and N is also a constant when the order of the Gaussian wavelet is selected. Only b determines the moment when $|X_g(\omega_h|a,b)|$ reaches maximum; therefore, we let the value of cos function be one. In this way, only the value of a controls the attenuation of the selected frequency components. Fig. 4(a) shows the features when a small value of a (less than four) is selected. One can see that the frequency coverage focuses on the high-frequency range, and amplification of these frequencies is low. When the
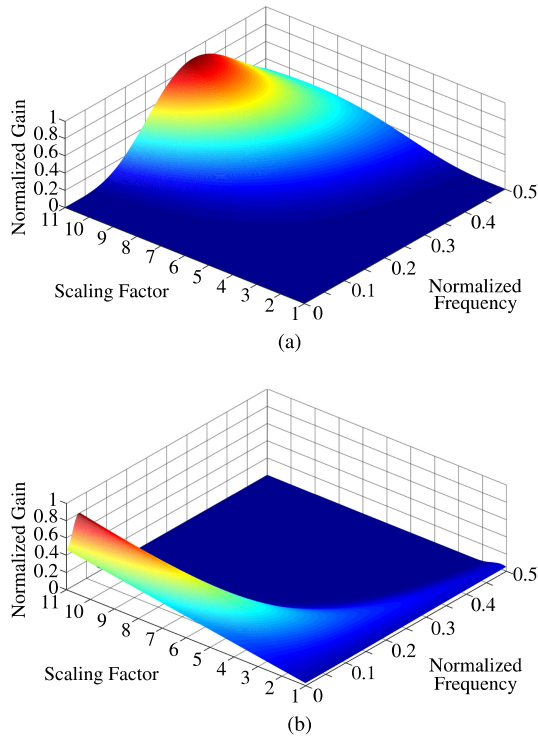
Fig. 4. Frequency coverage comparison of the WT between Gaussian wavelet and Morlet (normalized frequency f_h is used). (a) Gaussian. (b) Morlet.

value of a increases, the covered frequency range gets wider, and the amplification focuses on a certain range of the high frequency component. On the other hand, it has been proved that Fourier transform of a Gaussian waveform leads to another Gaussian curve in frequency domain. Similarly, when choosing a fixed value of a, the frequency coverage of a Gaussian wave is also a Gaussian-like curve. These characteristics are very suitable for feature extraction corresponding to a transformer saturation event, because the saturation waveform contains a Gaussian-like curve. Daughter wavelets with proper values of a could detect saturation and eliminate the influence of high frequencies. In contrast, the frequency coverage and the gain of the Morlet WT [see Fig. 4] mainly focus on low frequencies when a is greater than three. Even though it is a unilateral Gaussian-like curve with different value of a, the highlighted frequencies are low and suitable for feature extraction on the fundamental component. Detailed derivation of the Morlet WT for a sinusoidal waveform is shown in Appendix B. Therefore, we choose the Gaussian wavelet to be used in PCWT for the application of interest. Finally, the PCWT for feature extraction for GICs detection can be easily obtained by applying (6) to (12). All the parameter settings will be introduced in Section III-C.

B. GICs Detection by CNNs

The overall framework for the proposed detection mechanism is demonstrated in Fig. 5. First, PCWT with K number of a and STFT in L time instants are applied sequentially. Then, the scalogram and spectrogram will both be of $K \times L$ size and carry the valuable information on the intensity of GICs. The detection process could be converted as a supervised classification problem on the scalograms. However, the classification process for the 2-D scalograms is challenging due to their high dimensionality. Specifically, every frame of the obtained scalogram and spectrogram has hundreds by hundreds pixels; such high dimensional data is restrictive in most of the conventional pattern classification approaches. We cast the event detection (saturation caused by GICs) to an image classification problem based on the scalogram and spectrogram; we propose a CNN-based architecture to classify the images. The proposed CNN offers a simple architecture that ensures an accurate detection, yet fast and computationally effective. Our proposed CNN consists of five layers: three convolutional (Conv.) layers and two FC layers; the specifications of the CNN will be introduced in Section III-C. This framework can work as a standalone event detector or classification tool in a PMU to detect the GICs.

C. PCWT and CNN Parameter Setting

The sampling frequency used in this article is $Fs = 9600$ Hz, which is sufficiently high to cover up to 50th order of harmonics. The buffer size (observation window) for the PCWT and STFT are both set to 192 samples (20 ms). A Gaussian wavelet with order of 8 is employed. The time shifting b for all Gaussian daughter wavelets is set to be 10 ms (96 samples) for the sake of simplicity. The proposed scaling factor a for Gaussian wavelet is chosen as 2^i, where i is sampled among 256 uniform intervals in the range of $[-12, -4]$. The Gaussian mother wavelet has 20 ms duration, which is obtained by applying a unit length (1 s) Gaussian wavelet function into a 20 ms window. This transform is approximately equivalent to applying scaling factors from zero to eight with a mother wavelet of frequency 4000 Hz. Such selection of parameters reduces the computational burden associated with the scalogram acquisition, while does not sacrifice the bandwidth coverage for feature extraction. The scalograms have a duration of 40 ms (385 samples).

The proposed CNN for scalogram classification is illustrated in Fig. 5 with the following architecture: Input layer (256×385) – Convolutional (Conv.) layer ($100 \times 5 \times 11$) – Max-pooling layer (3×3) – Conv. layer ($100 \times 5 \times 5$) – Max-pooling layer (3×3) – Conv. layer ($64 \times 5 \times 5$) – FC layer (600×1) – FC layer (3×1). A wide-shape kernel is chosen in the first convolutional layer aiming to extract more information of the scalogram and spectrogram along the time axis. The stride of the convolution operation in the first layer is (2×3), while that of the other convolutional layers is (1×1). Batch normalization [40] is used in each Conv. and FC layers except the last FC layer. Dropout [41] is applied in the third Conv. layer and the first FC layer to prevent overfitting. Activation function used in the neural network is rectified linear unit (ReLU). Finally, Cross entropy is employed as the loss function.
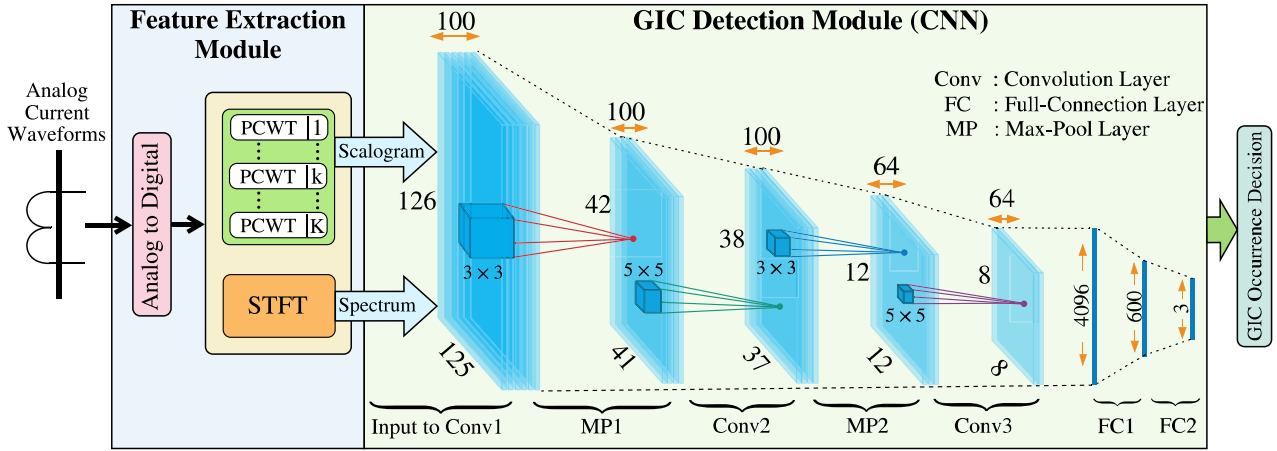
Fig. 5. General architecture of the proposed framework for GIC detection in power grids.

TABLE I
SIMULATED TEST WAVEFORM PARAMETER SPECIFICATION

Test Case	Saturation Type		
	AC	DC	NO
Saturation level	0.001pu-0.15pu	0.001pu-0.15pu	0
Harmonic Distortion	0.5 %-10 % THD; random choose up to 50th order		
Out-of-Band	10Hz to 120Hz; level 0.01pu-0.1pu		
Nonlinear Load	1% to 20% of total load		
Normal	Waveform from normal operating condition		

All generated signal has white Gaussian noise with same signal to noise ratio.

IV. CASE STUDY AND EXPERIMENTS

A. Test Scenarios Configuration

Three test cases are chosen from [42] to generate harmonics, aiming to simulate interferences in real-life power grid operating conditions and to facilitate the performance evaluations: harmonic distortions, out-of-band interferences, and harmonics from nonlinear loads. The parameter specifications of the test power waveforms for CNN training are shown in Table I. Three transformer saturation scenarios (ac saturation, dc saturation, and nonsaturation) are associated with four grid operating conditions (harmonic distortion, out-of-band interference, deployment of nonlinear loads, and normal operating condition). Therefore, 12 types of test waveforms are generated in total. All parameters are uniformly located in the designated ranges. Each type of event occurs within a 20 ms simulation runtime window randomly and individually. The transformer saturation model for waveform generation is obtained according to Fig. 2. Each type of the test waveform includes 1000 samples, and thus, a total of 12 000 samples (and wavelet scalogram and spectrogram) are simulated in the MATLAB environment, wherein 10 800 samples are used as the training dataset, 1200 samples for validation, and 6000 extra samples are generated for testing. All test waveforms are polluted by Gaussian noises at three levels of 20, 30, and 40 dB to approximate the thermal and measurement noises in different conditions. For training the neural network, Adam [43] was employed as the optimizer, which has the initial learning rates of 1×10^{-3}, $\beta_1 = 0.9$, and $\beta_2 = 0.999$. The

network was trained 120 epochs; in every 30 epochs, the learning rate decayed 1/10. The best validated model was recorded and tested.

B. Experimental Results and Analysis

Three patterns generated by PCWT for ac and dc saturation scenarios plus nonsaturation condition are demonstrated in Fig. 6. One can see that the scalograms generated by the proposed PCWT successfully reveal unique features in such scenarios: Fig. 6(b) shows consistent spikes indicating a full-cycle saturation. Fig. 6(c) shows one spike only that stands for a half-cycle saturation caused by GICs. In real-world operating conditions, the patterns in Fig. 6(a) can definitely affect the classification results during ac and dc saturation. The reason lies in the fact that the patterns in Fig. 6(a) would overlap those in Fig. 6(b) and (c), if harmonics and saturation occur at the same time. Therefore, the performance of CNN needs to be verified in such circumstances, in which the patterns are overlapped.

To verify the accuracy of the proposed solution under different GIC levels, a quantized test was conducted. The accuracy obtained from using PCWT, as well as using STFT, are compared with the proposed hybrid approach. The classification accuracy is tested for five quantized GIC intensity intervals shown in Table II. The highest accuracy in each scenario among the three tested approaches is highlighted. One can see that with same SNR, the detection accuracy increases as the GIC level intensifies. The proposed hybrid framework has the highest accuracy when SNR is low and the GIC intensity is weak. When SNR is high, the proposed PCWT could achieve a desirable accuracy.

In total, the proposed framework successfully achieves the best performance even under low-intensity GICs, high harmonics, and elevated noises. Moreover, the accuracy is still desirable if only using the proposed PCWT as the feature extraction tool. The framework works sufficiently fast, achieving the detection results within 30 ms (20 ms wavelet window plus 6.8 ± 2.7 ms the processing time); therefore, the framework can be applied for such online monitoring applications in power transmission systems.
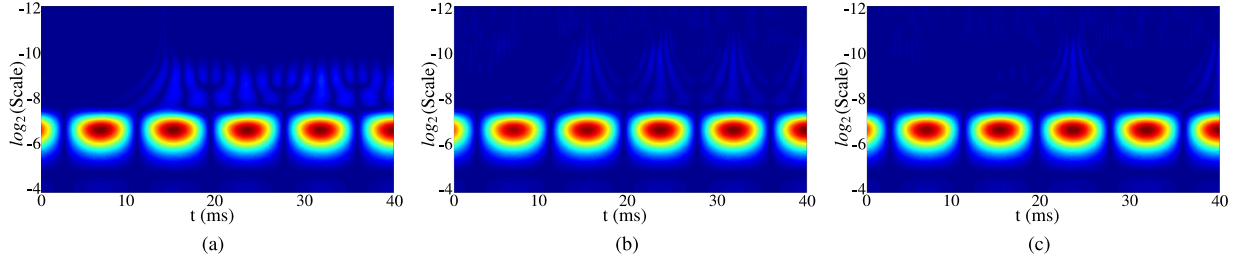
Fig. 6. Test waveform simulation results. (a) Polluted with random harmonics (nonsaturation with harmonics in the grid); (b) the equivalent AC saturation level of 0.01 p.u, and (c) the equivalent DC saturation level of 0.01 p.u.

TABLE II
ACCURACY PERFORMANCE OF THE TEST RESULTS

	GIC (pu)	0-0.03	0.03-0.06	0.06-0.09	0.09-0.12	0.12-0.15	Overall
	PCWT*	83.53%	90.66%	90.71%	90.54%	90.62%	88.97%
20dB	STFT	81.30%	90.34%	90.26%	90.38%	90.26%	88.32%
	Hybrid**	83.62%	90.68%	90.72%	90.55%	90.74%	88.99%
	PCWT*	88.75%	91.17%	91.15%	91.22%	86.87%	90.38%
30dB	STFT	87.47%	90.89%	91.02%	90.95%	90.95%	90.02%
	Hybrid**	88.77%	91.24%	91.28%	91.26%	91.30%	90.52%
	PCWT*	90.47%	91.49%	91.53%	91.54%	91.22%	90.95%
40dB	STFT	89.30%	91.22%	91.18%	91.26%	91.12%	90.45%
	Hybrid**	90.54%	91.47%	91.39%	91.53%	91.34%	90.92%

*:Proposed PCWT only. **:Proposed PCWT + STFT.

V. DISCUSSION AND CONCLUSION

This article aims to effectively detect GICs in power transmission systems during the GMD events. Our proposed approach consists of a hybrid feature extraction using Gaussian PCWT and STFT, and a CNN-based event detection mechanism. Experiments demonstrated that the proposed analytics achieved a high accuracy for online detection of GICs under different grid operating conditions. This framework would be installed within PMUs and/or other IEDs that can capture the power grid waveforms. Future work will focus on, first, applying the proposed framework to a variety of transformer saturation models, second, investigating the potential use of CNN or other machine learning algorithms for GICs measurements, and third, integrating the wavelet transformation into CNNs and simplifying the two-phase framework into one phase, which might further improve the realtime performance of the system.

APPENDIX A
DERIVATIONS OF THE GAUSSIAN WT

Using the definition presented in (9)

$$\int_{-\infty}^{\infty} g_1(x)dx = -g_0(x), \quad \int_{-\infty}^{\infty} g_n(x)dx = -g_{n-1}(x) \quad (16)$$

$$\int_{-\infty}^{\infty} g_n\left(\frac{t-b}{a}\right) d\left(\frac{t-b}{a}\right) = \frac{1}{a}\int_{-\infty}^{\infty} g_n\left(\frac{t-b}{a}\right) dt$$

$$= -g_{n-1}\left(\frac{t-b}{a}\right). \quad (17)$$

The first and second step partial integration of (10) is

$$X_g(w|a,b) \cdot \sqrt{C_{g_n}}$$

$$= -\left[ax(t)g_{n-1}\left(\frac{t-b}{a}\right)\right]_{-\infty}^{+\infty} + \int_{-\infty}^{\infty} \frac{d}{dt}x(t)ag_{n-1}\left(\frac{t-b}{a}\right)dt$$

$$= -\left[ax(t)g_{n-1}\left(\frac{t-b}{a}\right)\right]_{-\infty}^{+\infty} - \left[a^2\frac{d}{dt}x(t)g_{n-2}\left(\frac{t-b}{a}\right)\right]_{-\infty}^{+\infty}$$

$$+ \int_{-\infty}^{\infty} a^3\frac{d^2}{dt^2}x(t)g_{n-3}\left(\frac{t-b}{a}\right)dt$$

$$= \dots$$

$$= \sum_{n=0}^{N-1}\left[\left(-a^n\frac{d^n}{dt^n}x(t)\frac{d^{(N-n)}}{dt^{(N-n)}}g_0\left(\frac{t-b}{a}\right)\right]_{-\infty}^{+\infty}$$

$$+ \int_{-\infty}^{\infty} a^N\frac{d^N}{dt^N}x(t)g_0\left(\frac{t-b}{a}\right)dt. \quad (18)$$

By continuously applying the partial integration, (12) can be obtained. We know $g_n(\pm\infty) = 0$ and $\frac{d^n}{dt^n}x(t)$ is finite for any value of n; therefore, the summation in the first part in (12) would be zero.

APPENDIX B
DERIVATIONS OF THE MORLET WT

$$X_m(w|a,b) = \int_{-\infty}^{\infty} x(t) \frac{1}{\sqrt{\pi F_B}} \cos\left(\omega_c\left(\frac{t-b}{a}\right)\right) e^{-\frac{(t-b)^2}{a^2 F_B}} dt$$

$$= \int_{-\infty}^{\infty} A_h \cos(\omega_h t + \theta_h) \frac{1}{\sqrt{\pi F_B}} \cos\left(\omega_c\left(\frac{t-b}{a}\right)\right) e^{-\frac{(t-b)^2}{a^2 F_B}} dt \tag{19}$$
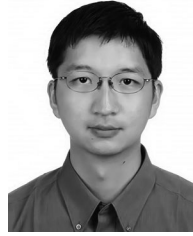
where $x = (t-b)/a$, F_B is a constant value representing the decay factor, and ω_c is the center frequency. Using the Euler's equation and (14), we can obtain

$$X_m(w|a,b)$$
$$= \frac{aA_h}{\sqrt{\pi F_B}} \int_{-\infty}^{\infty} \cos(a\omega_h x - \omega_h b + \theta_h) \cos(\omega_c x) e^{-\frac{x^2}{F_B}} dx$$
$$= \frac{aA_h}{2} \cos(a\omega_h + \theta_h)\left(e^{-\frac{F_B}{4}(a\omega_h + \omega_c)^2} + e^{-\frac{F_B}{4}(a\omega_h - \omega_c)^2}\right). \tag{20}$$

REFERENCES

[1] D. H. Boteler and R. J. Pirjola, "Modelling geomagnetically induced currents produced by realistic and uniform electric fields," *IEEE Trans. Power Del.*, vol. 13, no. 4, pp. 1303–1308, Oct. 1998.

[2] T. J. Overbye, T. R. Hutchins, K. Shetye, J. Weber, and S. Dahman, "Integration of geomagnetic disturbance modeling into the power flow: A methodology for large-scale system studies," in *Proc. North Amer. Power Symp.*, Sep. 2012, pp. 1–7.

[3] R. A. Walling, "Potential impacts of harmonics on bulk system integrity during geomagnetic disturbances," in *Proc. IEEE Power Energy Soc. General Meeting*, Jul. 2013, pp. 1–5.

[4] V. D. Albertson, J. M. Thorson, R. E. Clayton, and S. C. Tripathy, "Solar-induced-currents in power systems: Cause and effects," *IEEE Trans. Power App. Syst.*, vol. PAS-92, no. 2, pp. 471–477, Mar. 1973.

[5] X. Dong, Y. Liu, and J. G. Kappenman, "Comparative analysis of exciting current harmonics and reactive power consumption from GIC saturated transformers," in *Proc. IEEE Power Eng. Soc. Winter Meeting. Conf.*, Jan. 2001, vol. 1, pp. 318–322.

[6] A. Pulkkinen, S. Lindahl, A. Viljanen, and R. Pirjola, "Geomagnetic storm of 29–31 October 2003: Geomagnetically induced currents and their relation to problems in the Swedish high-voltage power transmission system," *Space Weather*, vol. 3, no. 8, pp. 1–19, Aug. 2005.

[7] S. Guillon, P. Toner, L. Gibson, and D. Boteler, "A colorful blackout: The havoc caused by auroral electrojet generated magnetic field variations in 1989," *IEEE Power Energy Mag.*, vol. 14, no. 6, pp. 59–71, Nov. 2016.

[8] J. Kappenman, *Geomagnetic Storms and Their Impacts on the US Power Grid.*, pp. 1–196, 2010.

[9] R. P. Medeiros and F. B. Costa, "A wavelet-based transformer differential protection with differential current transformer saturation and cross-country fault detection," *IEEE Trans. Power Del.*, vol. 33, no. 2, pp. 789–799, Apr. 2018.

[10] A. H. Etemadi and A. Rezaei-Zare, "Optimal placement of GIC blocking devices for geomagnetic disturbance mitigation," *IEEE Trans. Power Syst.*, vol. 29, no. 6, pp. 2753–2762, Nov. 2014.

[11] H. Zhu and T. J. Overbye, "Blocking device placement for mitigating the effects of geomagnetically induced currents," *IEEE Trans. Power Syst.*, vol. 30, no. 4, pp. 2081–2089, Jul. 2015.

[12] M. Kazerooni, H. Zhu, and T. J. Overbye, "Mitigation of geomagnetically induced currents using corrective line switching," *IEEE Trans. Power Syst.*, vol. 33, no. 3, pp. 2563–2571, May 2018.

[13] P. Ripka, K. Draxler, and R. Styblikova, "Measurement of dc currents in the power grid by current transformer," *IEEE Trans. Magn.*, vol. 49, no. 1, pp. 73–76, Jan. 2013.

[14] L. Lian-Guang, Z. Hao, L. Chun-Ming, G. Jian-Hui, and G. Qing-Xiong, "Technology of detecting GIC in power grids & its monitoring device," in *Proc. IEEE/PES Transmiss. Distrib. Conf. Expo., Asia Pacific.*, 2005, pp. 1–5.

[15] C. Rudin *et al.*, "Machine learning for the new york city power grid," *IEEE Trans. Pattern Anal. Mach. Intell.*, vol. 34, no. 2, pp. 328–345, Feb. 2012.

[16] S. Fan, L. Chen, and W.-J. Lee, "Machine learning based switching model for electricity load forecasting," *Energy Convers. Manage.*, vol. 49, no. 6, pp. 1331–1344, 2008.

[17] M. H. Rezaeian Koochi, P. Dehghanian, S. Esmaeili, P. Dehghanian, and S. Wang, "A synchrophasor-based decision tree approach for identification of most coherent generating units," in *Proc. Annu. Conf. IEEE Ind. Electron. Soc.*, Oct. 2018, pp. 71–76.

[18] S. Wang, P. Dehghanian, L. Li, and B. Wang, "A machine learning approach to detection of geomagnetically induced currents in power grids," in *Proc. IEEE Ind. Appl. Soc. Annu. Meeting*, 2019, pp. 1–7.

[19] N. A. E. R. Corporation, "Effects of geomagnetic disturbances on the bulk power system," 2012.

[20] J. A. de la O Serna and J. Rodríguez-Maldonado, "Taylor–Kalman–Fourier filters for instantaneous oscillating phasor and harmonic estimates," *IEEE Trans. Instrum. Meas.*, vol. 61, no. 4, pp. 941–951, Apr. 2012.

[21] M. Bertocco, G. Frigo, C. Narduzzi, C. Muscas, and P. A. Pegoraro, "Compressive sensing of a Taylor-Fourier multifrequency model for synchrophasor estimation," *IEEE Trans. Instrum. Meas.*, vol. 64, no. 12, pp. 3274–3283, Dec. 2015.

[22] Y.-C. Su, K.-L. Lian, and H.-H. Chang, "Feature selection of non-intrusive load monitoring system using STFT and wavelet transform," in *Proc. IEEE 8th Int. Conf. e-Business Eng.*, 2011, pp. 293–298.

[23] S.-H. Ni, K.-F. Lo, L. Lehmann, and Y.-H. Huang, "Time–frequency analyses of pile-integrity testing using wavelet transform," *Comput. Geotechnics*, vol. 35, no. 4, pp. 600–607, 2008.

[24] S. Wang, P. Dehghanian, and B. Zhang, "A data-driven algorithm for online power grid topology change identification with PMUs," in *Proc. IEEE Power Energy Soc. General Meeting*, Aug. 2019, pp. 1–5.

[25] D. P. Mishra, S. R. Samantaray, and G. Joos, "A combined wavelet and data-mining based intelligent protection scheme for microgrid," *IEEE Trans. Smart Grid*, vol. 7, no. 5, pp. 2295–2304, Sep. 2016.

[26] K. Thirumala, M. S. Prasad, T. Jain, and A. C. Umarikar, "Tunable-q wavelet transform and dual multiclass SVM for online automatic detection of power quality disturbances," *IEEE Trans. Smart Grid*, vol. 9, no. 4, pp. 3018–3028, Jul. 2018.

[27] P. Rajaraman, N. A. Sundaravaradan, R. Meyur, M. J. B. Reddy, and D. K. Mohanta, "Fault classification in transmission lines using wavelet multiresolution analysis," *IEEE Potentials*, vol. 35, no. 1, pp. 38–44, Jan. 2016.

[28] S. Wang, P. Dehghanian, and Y. Gu, "A novel multi-resolution wavelet transform for online power grid waveform classification," in *Proc. 1st IEEE Int. Conf. Smart Grid Synchronized Meas. Analytics*, May 2019, pp. 1–8.

[29] S. Wang, L. Li, and P. Dehghanian, "Power grid online surveillance through PMU-embedded convolutional neural networks," in *Proc. IEEE Ind. Appl. Soc. Annu. Meeting*, 2019, pp. 1–8.

[30] A. Krizhevsky, I. Sutskever, and G. E. Hinton, "ImageNet classification with deep convolutional neural networks," in *Proc. Adv. Neural Inf. Process. Syst.*, 2012, pp. 1097–1105.

[31] K. Simonyan and A. Zisserman, "Very deep convolutional networks for large-scale image recognition," Aug. 2014, *arXiv:1409.1556v6*.

[32] L. Li, M. Doroslovački, and M. H. Loew, "Discriminant analysis deep neural networks," in *Proc. 53rd Annu. Conf. Inf. Sci. Syst.*, Mar. 2019, pp. 1–6.

[33] I. Goodfellow, Y. Bengio, and A. Courville, *Deep Learning.* Cambridge, MA, USA: MIT Press, 2016. [Online]. Available: http://www.deeplearningbook.org

[34] Y. Bengio, A. Courville, and P. Vincent, "Representation learning: A review and new perspectives," *IEEE Trans. Pattern Anal. Mach. Intell.*, vol. 35, no. 8, pp. 1798–1828, Aug. 2013.

[35] T. Wiatowski, P. Grohs, and H. Bölcskei, "Energy propagation in deep convolutional neural networks," *IEEE Trans. Inf. Theory*, vol. 64, no. 7, pp. 4819–4842, Jul. 2018.

[36] T. Wiatowski and H. Bölcskei, "A mathematical theory of deep convolutional neural networks for feature extraction," *IEEE Trans. Inf. Theory*, vol. 64, no. 3, pp. 1845–1866, Mar. 2018.

[37] E. Oyallon, E. Belilovsky, and S. Zagoruyko, "Scaling the scattering transform: Deep hybrid networks," in *Proc. IEEE Int. Conf. Comput. Vision*, 2017, pp. 5618–5627.

[38] G. Ososkov and A. Shitov, "Gaussian wavelet features and their applications for analysis of discretized signals," *Comput. Phys. Commun.*, vol. 126, no. 1/2, pp. 149–157, 2000.

[39] J. Hubbard, "Calculation of partition functions," *Phys. Rev. Lett.*, vol. 3, no. 2, pp. 77, 1959.

[40] S. Ioffe and C. Szegedy, "Batch normalization: Accelerating deep network training by reducing internal covariate shift," Feb. 2015, *arXiv:1502.03167v3*.

[41] N. Srivastava, G. Hinton, A. Krizhevsky, I. Sutskever, and R. Salakhutdinov, "Dropout: A simple way to prevent neural networks from overfitting," *J. Mach. Learn. Res.*, vol. 15, no. 1, pp. 1929–1958, 2014.

[42] T. Becejac, P. Dehghanian, and M. Kezunovic, "Probabilistic assessment of PMU integrity for planning of periodic maintenance and testing," in *Proc. IEEE Int. Conf. Probab. Methods Appl. Power Syst.*, 2016, pp. 1–6.

[43] D. P. Kingma and J. Ba, "Adam: A method for stochastic optimization," Dec. 2014, *arXiv:1412.6980v9*.

Shiyuan Wang (S'18) received the B.Eng. degree in mechanical engineering from the University of Science and Technology, Beijing, China, in 2012, the M.Sc. degree in electrical engineering, in 2014, from The George Washington University, Washington, DC, USA, where he is currently working toward the Ph.D. degree with the Department of Electrical and Computer Engineering.

His research interests include power system reliability and resiliency, smart grid and renewable energy, power grid harmonic analysis, and application of signal processing in energy analytics.

Payman Dehghanian (S'11–M'17) received the B.Sc. degree from the University of Tehran, Tehran, Iran, in 2009, the M.Sc. degree from the Sharif University of Technology, Tehran, Iran, in 2011, and the Ph.D. degree from Texas A&M University, College Station, TX, USA, in 2017, all in electrical engineering.

He is currently an Assistant Professor with the Department of Electrical and Computer Engineering, The George Washington University, Washington, DC, USA. His research interests include power system protection and control, power system reliability and resiliency, asset management, and smart electricity grid applications.

Dr. Dehghanian is the recipient of the 2013 IEEE Iran Section Best M.Sc. Thesis Award in Electrical Engineering, the 2014 and 2015 IEEE Region 5 Outstanding Professional Achievement Awards, and the 2015 IEEE-HKN Outstanding Young Professional Award.

Li Li (S'18) received the B.Sc. degree in control engineering from Jilin University, Changchun, China, in 2008, the M.Sc. degree in electrical engineering from The George Washington University, Washington, DC, USA, in 2014, where he is currently working toward the Ph.D. degree with the Department of Electrical and Computer Engineering.

His research interests include image processing, artificial intelligence, and machine learning.

Bo Wang (S'15) received the B.Sc. degree in automation from Jilin University, Changchun, China in 2013, and the M.Sc. degree in electrical power and energy from The George Washington University, Washington, DC, USA, in 2015, where he is currently working toward the Ph.D. degree with the Department of Electrical and Computer Engineering.

His research interests include electric vehicles, power system optimization and control, and power system reliability.